Inverse Electrocardiography by Simultaneous Imposition of Multiple Constraints

Dana H. Brooks,* *Member, IEEE,* Ghandi F. Ahmad, Robert S. MacLeod, *Member, IEEE,* and George M. Maratos

***Abstract*—We describe two new methods for the inverse problem of electrocardiography. Both employ regularization with multiple constraints, rather than the standard single-constraint regularization. In one method, multiple constraints on the spatial behavior of the solution are used simultaneously. In the other, spatial constraints are used simultaneously with constraints on the temporal behavior of the solution. The specific cases of two spatial constraints and one spatial and one temporal constraint are considered in detail. A new method, the L-Surface, is presented to guide the choice of the required pairs of regularization parameters. In the case when both spatial and temporal regularization are used simultaneously, there is an increased computational burden, and two methods are presented to compute solutions efficiently. The methods are verified by simulations using both dipole sources and measured canine epicardial data.**

***Index Terms*—Electrocardiography, inverse problem, multiple constraints, regularization.**

I. Introduction

CHARACTERIZATION of electrophysiological cardiac events from standard electrocardiograms (ECG's) is often difficult because of sparse spatial sampling on the torso surface and attenuation and smoothing in the torso volume conductor. Clinically, this may lead to diagnostic ambiguities and compromised predictive abilities. One response to this ambiguity has been to employ technology that samples more of the available potential data on the body surface [1], [2] and to develop mathematical models that estimate cardiac activity from body surface potentials. These estimation techniques, known as solutions to the *inverse problem of electrocardiography*, require as a first step an explicit model of the volume conductor effects [3] which can predict body surface potentials from cardiac sources—i.e., a solution to the *forward problem*. Successful inverse solutions would enhance greatly the ability to detect, quantify, and localize cardiac activity from noninvasive surface measurements.

Manuscript received August 23, 1995; revised August 1, 1996, August 28, 1997, and January 13, 1998. This work was supported by the National Science Foundation under Grant BCS-9309359. *Asterisk indicates corresponding author.*

*D. H. Brooks is with the Communications and Digital Signal Processing (CDSP) Center, Electrical and Computer Engineering Department, Northeastern University, Boston, MA 02115 USA (e-mail: brooks@cdsp.neu.edu).

G. F. Ahmad is with the Electronics Engineering Department, College of Science and Technology, Al-Quds University, Abu-Deis, Jerusalem, Israel.

R. S. MacLeod is with the Cardiovascular Research and Training Institute (CVRTI), University of Utah, Salt Lake City, UT 84112 USA.

G. M. Maratos is with the Communications and Digital Signal Processing (CDSP) Center, Electrical and Computer Engineering Department, Northeastern University, Boston, MA 02115 USA.

Publisher Item Identifier S 0018-9294(99)00182-2.

Unfortunately, solutions to the inverse problem have to cope with a fundamental difficulty: due to attenuation, spatial smoothing, and discretization effects, the inverse problem is illposed [4], [5], i.e., small perturbations in the measured data or the forward solution produce unacceptably large errors in the inverse solutions. When, as is usually the case, the forward solution is represented as a matrix, the consequence of the illposedness is that the matrix will be illconditioned with a smooth spectrum of singular values. In order to overcome this instability, one usually applies an inverse procedure which selects the "best" solution from a restricted set of acceptable candidates. The most popular method to do so is regularization [6], [7]—an inverse solution is found as a particular tradeoff between a good fit to the data and the forward solution, on the one hand, and fidelity to an *a priori* constraint on candidate inverse solutions, on the other hand. This constraint is chosen for a combination of mathematical convenience and physical reasonableness, and forces the solution to be "reasonably small" or "reasonably smooth" on average, typically by constraining the two-norm of the amplitude (the "energy") or the two-norm of a derivative (e.g., a gradient or Laplacian estimate). In the ECG literature, regularization using a two-norm amplitude constraint is often referred to as Tikhonov zero-order, while regularization using the nth spatial derivative is called Tikhonov nth-order [4]. In the sequel we will use the terms energy regularization and Tikhonov zero-order regularization interchangeably.

This tradeoff between model fit and constraint is controlled by a multiplicative parameter known as the regularization parameter whose value is critical. The best choice depends on model and measurement error in a sensitive and complicated fashion, as has been shown both analytically in general [8] and experimentally for the electrocardiographic inverse problem [9], [10]. It can be chosen *a priori* but in most practical situations sufficient information to do so is not available—consequently a number of *a posteriori* methods have been developed for this purpose, such as combined residual and smoothing operator (CRESO) [11], the L-Curve [8], [12], and combined singular-value decomposition (SVD)-regularization methods [13], [14]. In most such techniques, solutions are calculated for a range of regularization parameters, and the "best" one is chosen as a good compromise between accuracy (residual error) and the particular method's criterion.

Unlike some inverse problems, where there may be a clear best choice of regularization constraint and parameter, the complicated nature of the equivalent source in the inverse problem of electrocardiography means that choosing any par-

ticular constraint has both advantages and disadvantages even with a "good" value of the regularization parameter. For example, solutions using a constraint on the two-norm of the solution may capture areas of large gradient such as activation wavefronts, but will tend to be noisy, while those using smoothness constraints based on spatial derivatives may be less noisy but may smear wavefronts [15], [16]. Standard regularized solutions to the inverse problem of electrocardiography have achieved only limited success; although the main features of epicardial potential distributions are roughly reconstructed, there is often considerable loss of accuracy with respect to both location and amplitude of extrema and wavefronts and spurious low-amplitude noise. Thus, the reliability of solutions is uncertain. Both choices, of regularizing function and of regularization parameter, require hard tradeoffs between smoothing and accuracy. In response to the limited success of these methods, in recent years researchers have looked for ways to incorporate additional *a priori* information into the solution. Some approaches constrain the forward solution, e.g., by "locally tuned" regularization of matrix factors of the forward solution representing relationships between particular surfaces or regions [17], or by rewriting the forward solution as a generalized eigenvalue problem with specific added constraints [18]. Others combine traditional regularization methods, such as truncated SVD and energy regularization [14].

In addition to the usual spatial constraints, there have also been limited attempts in the past to impose *temporal* constraints on the solution. The *a priori* knowledge that epicardial electrograms are temporally correlated is used to impose additional robustness against the spatial illcondition of the forward solution. Temporal constraints are not regularizers in the Tikhonov sense, directly combating the illposedness of the quasi-static (and, thus, spatial) inverse problem. Thus, one cannot successfully use temporal constraints without some regularization of the underlying spatial problem as well. But they are regularizers in the sense of being an attempt to impose constraints on solutions by restricting the acceptability of candidate solutions based on prior knowledge, and can be used in a regularization scenario known as Twomey regularization [19]. Previous attempts to use temporal information have involved either explicit or implicit constraints. Implicit methods have included reconstructing only the activation sequence, rather than the complete epicardial potential distribution [20], implying an on-off temporal model of electrograms, reformulated in terms of derivatives in the work of Greensite *et al.* [21]. Implicit temporal constraints also underlie a power-spectrum formulation of the inverse problem, using the minimum relative entropy reconstruction principle and autoregressive (AR) modeling, reported in [22]. Explicit use of temporal constraints received early attention in [23], but was recently revived in the work of Oster and Rudy (see, for example, [19]). In this work, temporal regularization was applied in a second step via a temporally smoothing post-filtering operation, after a first step of spatial regularization. Another explicit temporal regularization approach incorporates Kalman filtering in the constraint mechanism [24], [25]—this method imposes an explicit "forward" temporal model as well as the standard forward spatial model.

Recently, we have investigated methods which attempt to impose two spatial constraints [26] or a temporal and a spatial constraint [15] simultaneously. The estimate in our approach is the solution to a *joint* minimization problem over the fit error and the two constraints. The motivation for such an approach is threefold.

1) No *a priori* constraint is clearly superior from a physiological point of view, but several have physiological validity; therefore, we attempt to combine the advantages of two reasonable constraints and evaluate the results.
2) The imposition of constraints, although necessary to stabilize the problem, introduces a bias on the solution. By using more than one constraint, we hope to be able to reduce the severity of each constraint (i.e., use smaller individual regularization parameters) and, thereby, moderate this bias.
3) Typically, regularized solutions are quite sensitive to the value of the regularization parameter. By using two constraints we hope to increase robustness to changes in the values of the regularization parameters.

The drawbacks of such an approach include the need for two regularization parameters and possibly a large increase in the computational complexity of the problem.

II. Problem Formulation

In this section we describe the specific formulation of the forward and inverse problems of electrocardiography which we will use in the rest of the paper together with standard regularized solutions and methods to choose regularization parameters. We then present a general formulation of a multiple spatial regularization inverse problem and an augmented formulation that allows us to consider spatial and temporal constraints jointly.

A. Forward Model

In this work we used an epicardial potential distribution equivalent source model for reasons described in [4], [27], and [28]. Our geometric model consisted of epicardial and body surfaces (no internal surfaces were included), described by a set of nodes on each surface connected into triangles. The mathematical formulation was a discrete, quasi-static [29] approximation of Laplace's equation for the region between the heart and body surfaces with mixed boundary conditions of known epicardial potentials and a zero normal electric field at the body surface, solved numerically using boundary-element-method (BEM) techniques, following [4] and [30].

The resulting forward solution is a discrete model expressing the potential at each body surface node as a linear combination of the potentials at all the nodes of the epicardial surface. Enumerating the epicardial and body surface nodes and stacking them in vectors, we have

$$\boldsymbol{y}(k) = \boldsymbol{A} \cdot \boldsymbol{h}(k) + \boldsymbol{e}(k) \qquad k = 1, 2, \cdots, L \tag{1}$$

where $\boldsymbol{y}$ is the $M \times 1$ vector of torso potentials at time instant k, $\boldsymbol{h}(k)$ is the $N \times 1$ vector of epicardial potentials,

$\boldsymbol{A}$ is the $M \times N$ (usually $M > N$) matrix representing the forward solution, $\boldsymbol{e}$ is a measurement noise vector of the same dimensions as $\boldsymbol{y}$, and k and L are a discrete time index and the number of time samples, respectively.

The inverse problem, then, is to find $\hat{\boldsymbol{h}}$, an estimate of $\boldsymbol{h}$, given $\boldsymbol{A}$ and $\boldsymbol{y}$ at each time instant. Although $\boldsymbol{A}$ is assumed known, it is generally not square, is illconditioned and, as noted, has a gradually decaying spectrum of singular values.

B. Regularized Inverse Solutions

A standard least-square solution to (1) gives an estimate of the unknown vector $\boldsymbol{h}$ which will be extremely sensitive to the noise. Perturbations in the measurements will cause unstable oscillations in the inverse solution, and low-rank approximation of $\boldsymbol{A}$ via truncation of the singular value sequence will usually not give good results because of the lack of a clear threshold in the singular spectrum. Hence, there is a need for procedures to provide a stable solution.

1) Traditional Tikhonov Regularization: One common method of stabilizing the inverse solution is to use Tikhonov regularization [4], [7], [31]

$$\hat{\boldsymbol{h}}_\lambda = \arg\min_{\boldsymbol{x}} \left(||\boldsymbol{y} - \boldsymbol{A}\boldsymbol{x}||^2 + \lambda^2 ||\boldsymbol{R}\boldsymbol{x}||^2 \right) \tag{2}$$

where λ^2 is the regularization parameter and the $P \times N$ matrix $\boldsymbol{R}$ ($P \leq N$), represents a regularizing side constraint. In this formulation, if $\boldsymbol{R}$ is, for example, the identity matrix, the solution $\hat{\boldsymbol{h}}$, is the Tikhonov zero-order solution and is constrained in energy (l_2 norm). If $\boldsymbol{R}$ approximates the first or second spatial derivative, then $\hat{\boldsymbol{h}}$ is the Tikhonov first- or second-order solution, respectively, and is constrained to have a smooth surface gradient or curvature.

The solution to (2) is

$$\hat{\boldsymbol{h}}_\lambda = \left(\boldsymbol{A}^T\boldsymbol{A} + \lambda^2 \boldsymbol{R}^T\boldsymbol{R} \right)^{-1} \boldsymbol{A}^T\boldsymbol{y}. \tag{3}$$

Choice of Regularization Parameter: Many *a posteriori* techniques have been proposed to find regularization parameters. One which has been specifically proposed for the electrocardiographic inverse problem is the CRESO technique [11]. Here we have focused our attention on a standard method in the literature, the L-Curve, advocated for general discrete inverse problems by Hansen [12], because it can be expanded in a straightforward fashion to include multiple constraints (see Section III-B).

The L-Curve method requires the construction of a parametric graph, for many regularization parameters, of the (semi) norm $||\boldsymbol{R}\hat{\boldsymbol{h}}||_2$ of the regularized solution versus the corresponding residual (semi) norm $||\boldsymbol{y} - \boldsymbol{A}\hat{\boldsymbol{h}}||_2$. This graph, called the L-Curve, varies monotonically with the regularization parameter and has a characteristic L-shaped appearance (hence, its name) when plotted in *log-log* scale. The curve usually has a distinct corner separating the vertical and horizontal portions; this corner identifies a close-to-optimal regularization parameter. An example of an L-Curve for an electrocardiographic inverse solution is shown in Fig. 1. The first (vertical) part of the L-Curve corresponds to solutions, obtained with small values of λ, which are dominated by the side constraint error—$||\boldsymbol{R}\hat{\boldsymbol{h}}||_2$ increases sharply with decreasing λ while the residual norm decreases only slightly. In contrast, in the horizontal part of the L-Curve, obtained by over regularizing, $||\boldsymbol{R}\hat{\boldsymbol{h}}||_2$ only decreases a little with increasing regularization parameter while the residual error norm rises rapidly. The "×" in the figure marks the corner of the L-Curve, corresponding to a good choice for the regularization parameter. Changing the parameter from very close to this point on the curve will begin to either drastically increase the constraint error without significantly reducing the residual error or to drastically increase the residual error without significantly decreasing the constraint error. Thus, the L-Curve clearly demonstrates the tradeoff between minimizing the residual norm and minimizing the side constraint.

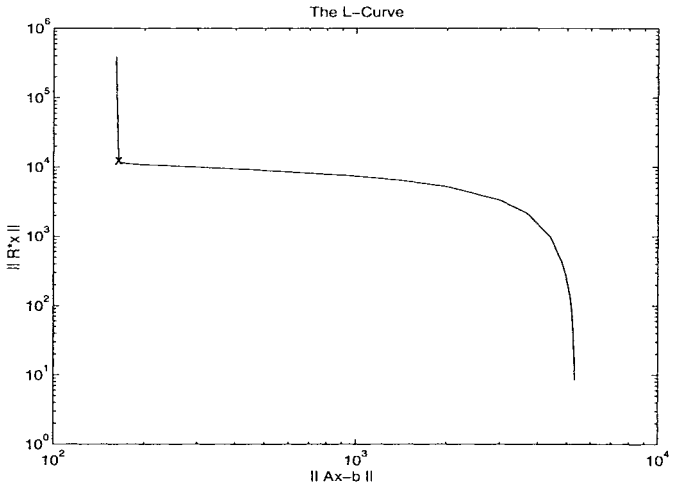

Fig. 1. An example of an L-Curve showing the solution norm as a function of the residual norm. This figure is based an inverse solution using the matrix $\boldsymbol{A}$ from the realistic human torso model, as described in Section IV with $\boldsymbol{R}$ the identity matrix.

C. Regularization with Two Constraints

1) Multiple Spatial Constraint Regularization: The minimization problem using k spatial constraints can be written as

$$\hat{\boldsymbol{h}}_\lambda = \arg\min_{\boldsymbol{x}} \left(||\boldsymbol{y} - \boldsymbol{A}\boldsymbol{x}||^2 + \sum_{i=1}^{k} \lambda_i^2 ||\boldsymbol{R}_i\boldsymbol{x}||^2 \right). \tag{4}$$

Note that each constraint employed requires its own regularization parameter λ_i.

2) Augmented Problem to Introduce Temporal Constraints: As described in Section I, several investigators have used the correlation between the temporal samples of electrograms to improve inverse solutions, notwithstanding the quasi-static nature of ECG propagation in the torso volume conductor. Our approach is based on the assumption that electrograms are reasonably correlated in time (or low pass in frequency). Although the temporal constraint here is not strictly a regularizer, we will refer to this approach as joint time/space (JTS) regularization.

We begin by defining an augmented forward model [13]

$$\overline{\boldsymbol{y}} = \overline{\boldsymbol{A}}\boldsymbol{h} + \overline{\boldsymbol{e}} \tag{5}$$

where $\overline{\boldsymbol{y}} \stackrel{\text{def}}{=} [\boldsymbol{y}^T(1), \cdots, \boldsymbol{y}^T(L)]^T$, $\overline{\boldsymbol{h}}$ and $\overline{\boldsymbol{e}}$ are defined similarly, $\overline{\boldsymbol{A}} \stackrel{\text{def}}{=} \boldsymbol{I}_L \otimes \boldsymbol{A}$, where $\otimes$ is the Kronecker product, $\boldsymbol{I}_L$ represents an $L \times L$ identity matrix, and L is the number of time samples included. Thus, $\overline{\boldsymbol{A}}$ is block diagonal and has the form

$$\overline{\boldsymbol{A}} = \begin{pmatrix} \boldsymbol{A} & \boldsymbol{0} & \boldsymbol{0} & \cdots & \boldsymbol{0} \\ \boldsymbol{0} & \boldsymbol{A} & \boldsymbol{0} & \cdots & \boldsymbol{0} \\ \boldsymbol{0} & \boldsymbol{0} & \boldsymbol{A} & \cdots & \boldsymbol{0} \\ & & & \cdots & \\ \boldsymbol{0} & \boldsymbol{0} & \boldsymbol{0} & \cdots & \boldsymbol{A} \end{pmatrix}. \tag{6}$$

An optimization problem which imposes a *joint* constraint in space (over the epicardial surface) and in time (over the time samples recorded at each sensor) can, then, be formulated as

$$\hat{\boldsymbol{h}} = \arg\min_{\overline{\boldsymbol{x}}} \cdot \left(\|\overline{\boldsymbol{A}}\overline{\boldsymbol{x}} - \overline{\boldsymbol{y}}\|^2 + \sum_{i=1}^{k_s} \lambda_i^2 \|\overline{\boldsymbol{R}}_i \overline{\boldsymbol{x}}\|^2 + \sum_{i=1}^{k_t} \eta_i^2 \|\overline{\boldsymbol{T}}_i \overline{\boldsymbol{x}}\|^2 \right). \tag{7}$$

We concentrate on the simplest case, one spatial and one temporal constraint, so that $k_s = k_t = 1$, and $\overline{\boldsymbol{R}}_1$ and $\overline{\boldsymbol{T}}_1$ are denoted as $\overline{\boldsymbol{R}}$ and $\overline{\boldsymbol{T}}$. $\overline{\boldsymbol{R}} \stackrel{\text{def}}{=} \boldsymbol{I}_L \otimes \boldsymbol{R}$ has the same structure as $\overline{\boldsymbol{A}}$, repeating the spatial regularization constraint at each time instant (note that in principle this regularization can be made time varying), and $\overline{\boldsymbol{T}}$, defined as $\overline{\boldsymbol{T}} \stackrel{\text{def}}{=} \boldsymbol{T} \otimes \boldsymbol{I}_N$, has the following block-Toeplitz structure with Toeplitz (and diagonal) blocks:

$$\overline{\boldsymbol{T}} = \begin{pmatrix} t_0 \boldsymbol{I}_N & t_1 \boldsymbol{I}_N & \cdots & t_{L-1} \boldsymbol{I}_N \\ t_{-1} \boldsymbol{I}_N & t_0 \boldsymbol{I}_N & \cdots & t_{L-2} \boldsymbol{I}_N \\ & & \cdots & \\ t_{-(L-1)} \boldsymbol{I}_N & t_{-(L-2)} \boldsymbol{I}_N & \cdots & t_0 \boldsymbol{I}_N \end{pmatrix}. \tag{8}$$

Thus, $\overline{\boldsymbol{T}}$ picks out the same time instant from all sensors and constrains temporal behavior according to the rows of $\boldsymbol{T}$. These rows can be seen as discrete estimates of a temporal derivative operator or as unit sample responses of high-pass filters. In the latter interpretation, $\boldsymbol{T}$ becomes the corresponding convolution matrix. The temporal filters can be made space varying, i.e., $\boldsymbol{T}$ can be a non-Toeplitz matrix, and time varying, in which case $\overline{\boldsymbol{T}}$ is not block Toeplitz.

III. Solution Approaches

In this section, we first present the solutions to the joint regularization problems formulated in the previous section. These solutions require the choice of two regularization parameters, and we next describe an extension of the L-Curve technique to the two parameter case. Finally, the problem size of the augmented time/space regularization problem grows linearly with the number of time samples included and, thus, there is an increase in the computational load for the solution of the associated system of equations which is cubic in L. In the last part of this section we present two techniques which, under certain conditions, allow an efficient solution to this augmented system of equations.

A. Forms of the Solution for Joint Regularization

In the case of multiple spatial regularization (4), the solution can be written as

$$\hat{\boldsymbol{h}}_\lambda = \left[\boldsymbol{A}^T\boldsymbol{A} + \sum_{i=1}^{k} \lambda_i^2 \boldsymbol{R}_i^T \boldsymbol{R}_i \right]^{-1} \boldsymbol{A}^T \boldsymbol{y}. \tag{9}$$

Thus, the solution for regularization with two spatial constraints is

$$\hat{\boldsymbol{h}}_\lambda = \left(\boldsymbol{A}^T\boldsymbol{A} + \lambda_1^2 \boldsymbol{R}_1^T \boldsymbol{R}_1 + \lambda_2^2 \boldsymbol{R}_2^T \boldsymbol{R}_2 \right)^{-1} \boldsymbol{A}^T \boldsymbol{y}. \tag{10}$$

For the case of the augmented time/space problem (7), the solution is

$$\hat{\overline{\boldsymbol{h}}} = \left(\overline{\boldsymbol{A}}^T\overline{\boldsymbol{A}} + \sum_{i=1}^{k_s} \lambda_i^2 \overline{\boldsymbol{R}}_i^T \overline{\boldsymbol{R}}_i + \sum_{i=1}^{k_t} \eta_i^2 \overline{\boldsymbol{T}}_i^T \overline{\boldsymbol{T}}_i \right)^{-1} \overline{\boldsymbol{A}}^T \overline{\boldsymbol{y}}. \tag{11}$$

For $k_s = k_t = 1$ the solution can be written

$$\begin{aligned} \hat{\overline{\boldsymbol{h}}} &= \left(\overline{\boldsymbol{A}}^T\overline{\boldsymbol{A}} + \lambda^2 \overline{\boldsymbol{R}}^T\overline{\boldsymbol{R}} + \eta^2 \overline{\boldsymbol{T}}^T\overline{\boldsymbol{T}} \right)^{-1} \overline{\boldsymbol{A}}^T \overline{\boldsymbol{y}} \\ &= \left[\boldsymbol{I}_L \otimes \left(\boldsymbol{A}^T\boldsymbol{A} \right) + \lambda^2 \boldsymbol{I}_L \otimes \boldsymbol{R}^T\boldsymbol{R} + \eta^2 \left(\boldsymbol{T}^T\boldsymbol{T} \right) \otimes \boldsymbol{I}_N \right]^{-1} \\ &\quad \cdot \left(\boldsymbol{I}_L \otimes \boldsymbol{A}^T \right) \overline{\boldsymbol{y}}. \end{aligned} \tag{12}$$

In the filtering interpretation of the matrix $\boldsymbol{T}$ described in Section II-C, the rows of the matrix $\boldsymbol{T}^T\boldsymbol{T}$, from which $\overline{\boldsymbol{T}}^T\overline{\boldsymbol{T}}$ is constructed, contain the deterministic autocorrelation sequence of the filter unit sample response.

B. Choice of Regularization Parameter Pair: The L-Surface

To solve either of these joint regularization schemes it is necessary to have a method to choose the values of the pair of regularization parameters $\underline{\lambda} \stackrel{\text{def}}{=} (\lambda_1, \lambda_2)$ or $\underline{\lambda} \stackrel{\text{def}}{=} (\lambda, \eta)$. Previously known methods are limited to only one parameter, so we have developed a new method based on the L-Curve, which we have denoted the L-Surface [15], [26]. Determining three or more parameters is beyond the scope of currently available methods and, thus, in this paper we deal only with two simultaneous constraints. The L-Surface is applicable both to regularization with two spatial constraints on a time-instant-by-time-instant basis and to the JTS problem in the augmented problem space. The L-Surface is drawn by plotting the residual norm against the two side constraint norms for each pair of regularization parameters, thus forming a surface as a bivariate parametric function of the regularization parameter pair. The "corner" of this surface then indicates an estimate of a good regularization parameter pair.

C. Efficient Solutions to the Augmented Problem

As mentioned above, the size of the augmented scheme (12) is critical. As the number of time instants increases, standard block solutions quickly become prohibitive. This is especially true if we employ *a posteriori* techniques such as the L-Surface to obtain a good $\underline{\lambda}$ as we then have to solve (12) many times for each inverse solution. However, the matrix is highly structured: it is a positive definite sparse symmetric matrix, nonzero only in the diagonal blocks and along the

diagonals of some off-diagonal blocks. Under certain conditions, this structure allows us to achieve efficient solutions via either iterative or diagonalization techniques. The iterative scheme, in addition to being computationally more efficient than a direct solution, has an interpretation which allows us to track a progression of inverse solutions; we go from a standard, spatial-only regularization, to a first-step solution obtained by post-filtering of the spatially regularized solution (similar to the method in [19]), through a series of increasing degrees of temporal filtering, until we converge to the jointly optimal solution to (12). The diagonalization method when the spatial regularization is Tikhonov zero order is even more efficient than the iterative scheme, especially when multiple solutions are required (as when constructing an L-Surface), since it requires only one diagonalization each of the "small" matrices $\boldsymbol{A}$ and $\boldsymbol{T}$, followed for any $\underline{\lambda}$ by scalar and matrix multiplications only.

1) Block Jacobi Iterative Scheme: Writing (12) as

$$\begin{aligned}\left[\boldsymbol{I}_L \otimes \left(\boldsymbol{A}^T\boldsymbol{A}\right) + \lambda^2 \boldsymbol{I}_L \otimes \left(\boldsymbol{R}^T\boldsymbol{R}\right) + \eta^2\left(\boldsymbol{T}^T\boldsymbol{T}\right) \otimes \boldsymbol{I}_N\right]\hat{\overline{\boldsymbol{h}}} \\ = \left(\boldsymbol{I}_L \otimes \boldsymbol{A}^T\right)\overline{\boldsymbol{y}}\end{aligned} \tag{13}$$

we can denote this system as

$$\overline{\boldsymbol{B}} \cdot \hat{\overline{\boldsymbol{h}}} = \overline{\boldsymbol{b}}. \tag{14}$$

The matrix $\overline{\boldsymbol{B}}$ has a block structure

$$\overline{\boldsymbol{B}} = \begin{pmatrix} \boldsymbol{B}_{11} & \boldsymbol{B}_{12} & \cdots & \boldsymbol{B}_{1L} \\ \boldsymbol{B}_{21} & \boldsymbol{B}_{22} & \cdots & \boldsymbol{B}_{2L} \\ \cdots & \cdots & \cdots & \cdots \\ \boldsymbol{B}_{L1} & \boldsymbol{B}_{L2} & \cdots & \boldsymbol{B}_{LL} \end{pmatrix} \tag{15}$$

where the $\boldsymbol{B}_{ij}$ blocks are square matrices of size $N \times N$. The diagonal blocks are well conditioned due to regularization. If the vectors $\hat{\overline{\boldsymbol{h}}}$ and $\overline{\boldsymbol{b}}$ are divided into blocks accordingly, the ith block equation can be written

$$\boldsymbol{B}_{ii}\hat{\overline{\boldsymbol{h}}}_i + \sum_{j \neq i} \boldsymbol{B}_{ij}\hat{\overline{\boldsymbol{h}}}_j = \boldsymbol{b}_i. \tag{16}$$

Thus, we can solve for $\hat{\overline{\boldsymbol{h}}}_i$ as

$$\hat{\overline{\boldsymbol{h}}}_i = \boldsymbol{B}_{ii}^{-1}\left(\boldsymbol{b}_i - \sum_{j \neq i} \boldsymbol{B}_{ij}\hat{\overline{\boldsymbol{h}}}_j\right). \tag{17}$$

The problem in implementing this last equation is that we need the unknown values of the other block vectors $\hat{\overline{\boldsymbol{h}}}_j$ to find $\hat{\overline{\boldsymbol{h}}}_i$. A "natural" iterative scheme would be to proceed as follows: At the $(k+1)$st iteration, set

$$\hat{\overline{\boldsymbol{h}}}_i^{(k+1)} = \boldsymbol{B}_{ii}^{-1}\left(\boldsymbol{b}_i - \sum_{j \neq i} \boldsymbol{B}_{ij}\hat{\overline{\boldsymbol{h}}}_j^{(k)}\right) \qquad (i = 1, 2, \cdots, L) \tag{18}$$

initialized by $\hat{\overline{\boldsymbol{h}}}_i^{(0)} = \boldsymbol{B}_{ii}^{-1}\boldsymbol{b}_i$ (i.e., the usual spatially regularized solution with some additional two-norm regularization due to the zeroth lag of the filter autocorrelation sequence).

This scheme can be interpreted as initially solving a spatial system only, then at each iteration, for each time instant, resolving the combined problem using results of the previous iterations in the temporal filter. Under what conditions will this scheme converge to the correct minimum of the augmented problem? It can be shown that this scheme is of the block Jacobi type [32] and that the matrix $\overline{\boldsymbol{B}}$ has to have *block* diagonal dominance to guarantee convergence. This turned out to be the case for all our tests; more detail on convergence conditions can be found in Appendix A. This iterative solution reduces the computational complexity to the same order as the single time instant case. Its speed of convergence is a function of the degree to which the diagonal block matrices dominate. The convergence conditions can be determined directly, or at least bounded, in terms of the coefficients of the temporal filter (since the matrices $\boldsymbol{B}_{ij}$ are diagonal) and the magnitude of the regularization parameters.

2) Pre/Post Diagonalization Scheme: An even more computationally efficient solution to (12) can be achieved for the case of Tikhonov zero-order spatial regularization ($\boldsymbol{R} = \boldsymbol{I}$) by a pre/post diagonalization method adapted from a method described for a different problem in [33]. This method requires one-time diagonalizations of two matrices whose sizes are of the order of the spatial and temporal size of the problem respectively, followed by simple matrix multiplication.

The solution depends on noticing that (13) can be written as

$$\boldsymbol{P}\boldsymbol{H} + \boldsymbol{H}\boldsymbol{S} = \boldsymbol{Z} \tag{19}$$

where $\boldsymbol{P} = (\boldsymbol{A}^T\boldsymbol{A}) + \lambda^2(\boldsymbol{R}^T\boldsymbol{R})$, and $\boldsymbol{S} = \eta^2(\boldsymbol{T}^T\boldsymbol{T})$, $\boldsymbol{H}$ is a matrix of the unknown epicardial potentials with rows and columns as its spatial and temporal dimensions, respectively (i.e., the ith row of $\boldsymbol{H}$ is the desired unknown time signal at the ith epicardial node and the jth column of $\boldsymbol{H}$ contains the desired epicardial potentials at time j), and $\boldsymbol{Z} = \boldsymbol{A}^T\boldsymbol{Y}$, where $\boldsymbol{Y}$ contains the known data on the torso surface organized in an analogous fashion to $\boldsymbol{H}$. Details of the solution are given in Appendix A. The key advantage of this approach is that if $\boldsymbol{R} = \boldsymbol{I}$, we only need to decompose the "small" matrices $\boldsymbol{A}$ and $\boldsymbol{T}$ once; solutions for many different regularization pairs require only scalar operations and matrix multiplication. If $\boldsymbol{R} \neq \boldsymbol{I}$, then we can still use this approach but we would need to decompose the matrix $\boldsymbol{P}$ separately for each value of λ.

IV. Results and Discussion

A. Simulation Experiments

We have applied the methods discussed in this paper to simulated torso data and numerical forward solutions from two different heart/torso and source models. In one model, a single dipole was used to simulate the source of epicardial and torso potentials. In the other model, measured epicardial potentials served as an equivalent source for generating torso potentials. In both cases, the geometrical model was treated as homogeneous between the epicardial and torso surfaces, torso surface potentials were simulated as described below, Gaussian white noise was added to the forward computed torso data at specified signal-to-noise ratios (SNR's), and from these data we estimated epicardial potentials.

1) Dipole Model: The geometric model for this forward solution was based on a human subject (the Dalhousie torso [16]) and consisted of 352 torso nodes connected to form 700 triangles and 98 epicardial nodes connected to form 192 triangles. The cardiac source was a single dipole located near the center of the ventricles from which we calculated both epicardial and torso surface potentials by two different numerical pathways.

a) We computed both epicardial and torso potentials directly from the dipole source.
b) We computed epicardial potentials from the dipole as above, and then, using these computed epicardial potentials as an equivalent source, we used the forward solution matrix $\boldsymbol{A}$ to compute the torso potentials.

In the second path, we computed the torso potential using the same forward matrix $\boldsymbol{A}$ used in the inverse solution; hence, we have exactly complementary or *matched* conditions. The first path, on the other hand, produces slightly different torso potentials, computed without using the matrix $\boldsymbol{A}$, resulting in a *model mismatch* that is more representative of any practical application of the inverse solution. Neither case is an exact forward solution, of course, and both have bias. However, robustness to this type of model mismatch is an important attribute for which inverse solution methods should be tested.

Three orientations of the dipole were used, aligned with the X-, Y-, and Z-axes of the torso geometry, in addition to linear combinations of these three orientations. In each case, the epicardial potentials computed from the dipole source were the true solution against which inverse solutions were evaluated. One major limitation of the dipole experiments is that it is difficult to reproduce realistically complex epicardial potential distributions due to the simplicity of the model. A second is that there is no natural way to produce realistic simulations of the time-varying epicardial distributions needed to test the JTS method.

2) Tank Preparations: To test our inverse methods using realistic time-varying data, we used epicardial data recorded at the Cardiovascular Research and Training Institute (CVRTI), University of Utah, Salt Lake City, from an isolated canine heart preparation during experiments conducted as part of other projects. The heart was suspended in a fiberglass tank molded in the shape of an adolescent human torso and filled with electrolytic solution at a resistivity of 500 Ω-cm, representative of a typical torso volume conductor. Circulation was provided via cannulation and retrograde perfusion of the aorta by a support dog. Epicardial potentials were recorded at a sampling rate of 1000 Hz/channel via 64 electrodes sewn into a nylon sock placed over the suspended heart [34]. The heart was paced by one of the sock electrodes or by means of a hook electrode in the right atrium. From each acquisition epoch of 4–7 s of potentials we averaged over 5–8 sequential, time aligned, beats to derive a representative beat for each epoch. Simulated potentials at 658 torso surface nodes were computed using a forward model based on a BEM solution for a nominal heart location within the tank geometry.

3) Error Measures: We report error measures which are standard in the literature, namely, relative mean square error (RMSE) and correlation coefficients (CC) [4]. Although global error measures such as RMSE and CC are incomplete, there is currently a dearth of accepted and physiologically based *quantitative* measures based on features of the potential distributions. Thus, the literature on inverse solutions tends to rely on RMSE and CC. To partially alleviate this problem we also present several figures showing epicardial time signals (electrograms) and isopotential maps (IPM's) [1], [35] of original data and inverse-computed solutions, so that the reader can visually compare the quality of the results. The format for the IPM's is a polar projection with the apex of the heart in the center and the atrioventricular ring around the outside [16], [34], as illustrated in Fig. 2. The problem of illustrating and quantifying results is compounded for the case of joint spatial and temporal reconstruction by the need to present a temporal sequence of IPM's of sufficient length to be able to properly evaluate the results. Readers who wish to see more detail of the results are encouraged to see [36], as well as an animation of one simulation, both available at: http://www.cdsp.neu.edu/info/faculty/brooks/brooks.html.

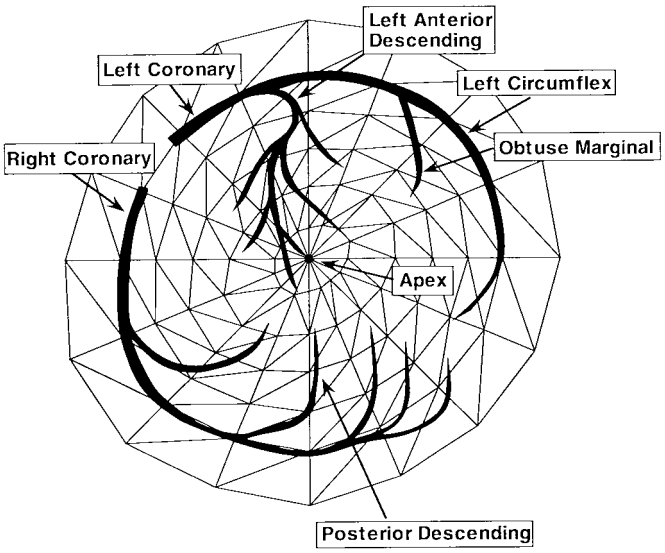

Fig. 2. Polar projection of the epicardium used for plotting IPM's of epicardial potential distributions.

B. Results

We describe specific results using the L-Surface and inverse solutions computed using joint regularization with 1) two constraints and 2) a spatial constraint coupled with a temporal constraint.

1) Estimation of Regularization Parameters—the L-Surface: To determine the regularization coefficient pairs required for both joint spatial and joint time-space regularization we calculated the L-Surface over a reasonable range of regularization parameters. Fig. 3 depicts a typical L-Surface for joint time and space regularization. The upper figure shows the surface over a wide range of regularization parameters and the bottom figure is an enlargement of the corner where good regularization parameter pairs are located. As indicated by the labels on the upper figure, the horizontal axis is

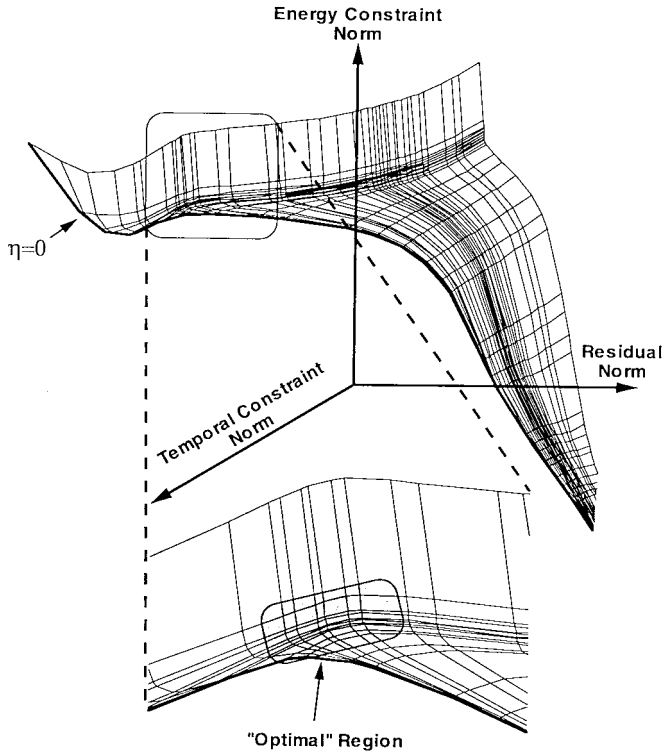

Fig. 3. The L-Surface: an extension to the L-Curve, showing the log of the two-norms of the two constraint terms as a function of the log of the residual norm over a range of values of the parameter pair (λ, η), constructed from torso tank data. The upper figure illustrates the surface over a wide variety of regularization parameters, while the lower figure is an enlargement of the "corner" where good regularization parameters are localized. The format of the figure is described in the text.

the residual norm, the vertical axis is the spatial constraint norm, and the axis coming out of the page is the temporal constraint norm, all plotted on a log scale. The $\boldsymbol{A}$ matrix used was the transformation matrix from the tank experiment described in Section IV-A, the spatial constraint was an energy constraint, and the temporal constraint was the one given in Section IV-B3. To draw the figure, we connected line segments between points with constant temporal regularization parameter as the spatial regularization parameter (λ) changed, and then connected line segments between points of constant spatial regularization parameter as the temporal regularization parameter (η) changed. Thus, every intersection in the figure corresponds to a particular (λ, η) pair. The standard Tikhonov zero-order $(\eta = 0)$ solution corresponds to the "front-most" such line, (i.e., the front edge of the surface, enhanced in the figure) and as the temporal regularization parameter increases the curves progress into the plane of the paper. The shaded region labeled "optimal region" in the figure is the "corner" of the L-Surface—the region analogous to the corner of the traditional L-curve for a single regularization constraint. L-Surfaces for the joint spatial regularization method were similar, although narrower, due to fact, already explained, that both constraints were true spatial regularizers.

There are several aspects of joint regularization which can be observed by inspection of Fig. 3 and which are typical of the L-Surfaces we have studied.

a) *Robustness:* The density of intersections is greater near the optimal region than along the $\eta = 0$ line. In the left (front) portion of the L-Surface plot one can see that the spacing between intersections along each constant temporal regularization parameter curve, which reflects the sensitivity of the regularization to the choice of η, was considerably smaller in the optimal region than near the $\eta = 0$ edge. The change in error norms with regularization parameter was smaller in the optimal region than for smaller values of η, even for an optimal choice of λ. The four values of the spatial regularization parameter which correspond to the center of the optimal region range in value from 5×10^{-7} to 1×10^{-5}.

b) *Better definition of the corner of the surface:* moving from the $\eta = 0$ edge toward the optimal zone, the corner became sharper with increasing values of the η, even as more intersection points moved into the corner. The combined result is that through the presence of the second constraint, it becomes easier to locate the optimal region and less critical to select its center.

c) *Less weight on the spatial constraint norm:* The optimal region occurred at smaller values of the energy regularization parameter than the corner of the $\eta = 0$ edge.

This observation indicates less "bias" in the solution imposed by the joint constraint norms, compared to only the energy norm, for a comparable level of stability. Comparisons are made here to the $\eta = 0$ case (only a spatial constraint) but not to the $\lambda = 0$ case (only a temporal constraint) because of the fact that the temporal constraint by itself is not a regularizer, as explained in Section I.

In all the tests we performed for joint inverse procedures, the "corner" of the L-Surface showed less sensitivity to changes in either regularization parameter than did the corresponding single regularization L-Curves. This indicates that with joint regularization the norms of inverse solutions are more robust to error in the choice of regularization parameters. As we illustrate below, in our experience not only the norms but also the solutions themselves are more robust.

2) Joint Spatial Regularization: We combined Tikhonov zero-order and Tikhonov second-order constraints in our test. Thus, in (10) we took $\boldsymbol{R}_1$ as the identity matrix, to constrain the solution in energy (l_2 norm), and $\boldsymbol{R}_2$ as the second spatial derivative (Laplacian) to constrain $\hat{\boldsymbol{h}}$ to be smooth.[1] Inverse epicardial potentials were calculated from body surface potentials for both types of data sets at various levels of SNR.

a) Dipole results with and without model mismatch: As described above, we generated two types of body surface potentials, with and without model mismatch between forward and inverse models, using the human torso geometry. We added noise at three SNR levels and then used Tikhonov zero-order regularization, Tikhonov second-order regularization, and joint solutions using both regularization constraints, and calculated inverse solutions over a wide range of regularization

[1] The Laplacian for our geometry was estimated using a method developed for an irregular triangular mesh on a three-dimensional surface [37].

TABLE I
THE RMSE FOR JOINT SPATIAL REGULARIZATION USING DIPOLE DATA WITH NO MODEL MISMATCH, 40-dB SNR. THE FIRST ROW IS THE LAPLACIAN REGULARIZATION PARAMETER AND THE FIRST COLUMN IS THE ENERGY REGULARIZATION PARAMETER

	0e-0	5e-3	1e-1	1e-0	1.5e1	6.0e1	8.0e1	1.0e2	2.5e2
0e-0	282.0	1.104	0.379	0.128	0.074	0.100	0.108	0.115	0.128
1e-6	1.050	0.683	0.350	0.127	**0.074**	0.100	0.108	0.115	0.128
5e-6	0.410	0.396	0.286	0.124	0.074	0.100	0.108	0.115	0.128
1e-5	0.309	0.304	0.243	0.120	0.074	0.100	0.108	0.115	0.128
5e-5	0.168	0.167	0.151	0.105	0.077	0.101	0.109	0.116	0.129
1e-4	0.141	0.140	0.131	0.102	0.080	0.103	0.111	0.117	0.130
5e-4	0.147	0.143	0.140	0.129	0.109	0.118	0.123	0.127	0.138
1e-3	0.162	0.162	0.161	0.154	0.135	0.135	0.138	0.141	0.148
5e-3	0.232	0.232	0.232	0.230	0.219	0.211	0.209	0.209	0.208
1e-4	0.270	0.270	0.270	0.269	0.262	0.254	0.253	0.252	0.250
5e-2	0.380	0.381	0.381	0.381	0.379	0.376	0.375	0.371	0.371
1e-1	0.440	0.440	0.440	0.440	0.440	0.438	0.437	0.437	0.436
2e-1	0.510	0.510	0.510	0.510	0.510	0.509	0.509	0.509	0.508
1e-0	0.727	0.727	0.727	0.727	0.727	0.727	0.727	0.727	0.727
2e-0	0.913	0.913	0.913	0.913	0.913	0.913	0.913	0.913	0.913

TABLE II
SAME FORMAT AS TABLE I FOR DIPOLE DATA WITH MODEL MISMATCH

	0e-0	5e-3	1e-1	1e-0	1.5e1	6.0e1	8.0e1	1.0e2	2.5e2
0e-0	713.00	2.68	0.975	0.406	0.193	0.151	0.149	0.149	0.153
1e-6	2.027	1.752	0.915	0.403	0.192	0.151	0.149	0.149	0.153
5e-5	1.108	1.066	0.760	0.392	0.192	0.150	0.149	0.149	0.153
1e-5	0.835	0.817	0.650	0.379	0.191	0.150	0.149	0.149	0.153
5e-5	0.420	0.418	0.396	0.318	0.186	0.149	0.148	0.148	0.152
1e-4	0.331	0.330	0.322	0.282	0.180	0.147	0.146	0.147	0.152
5e-4	0.218	0.218	0.215	0.204	0.160	**0.142**	0.143	0.144	0.150
1e-3	0.194	0.194	0.193	0.185	0.157	0.144	0.145	0.146	0.151
5e-3	0.216	0.216	0.216	0.214	0.203	0.194	0.193	0.192	0.192
1e-2	0.252	0.252	0.252	0.251	0.243	0.236	0.234	0.233	0.231
5e-2	0.366	0.366	0.366	0.366	0.364	0.360	0.359	0.359	0.357
1e-1	0.427	0.427	0.427	0.427	0.426	0.425	0.424	0.423	0.422
2e-1	0.500	0.500	0.500	0.500	0.499	0.498	0.498	0.498	0.497
1e-0	0.722	0.722	0.722	0.722	0.722	0.722	0.722	0.722	0.722
5e-0	0.912	0.912	0.912	0.912	0.912	0.912	0.912	0.912	0.912

parameter pairs. At all SNR's tested, the lowest relative error and highest correlation coefficient were obtained with joint spatial regularization. However, the improvement was often not very large. RMSE results for a selection of regularization parameter pairs are shown in Tables I and II, for the exact and mismatched model cases, respectively. The results of these tests led us to the following set of observations.

i) Inverse solutions using Laplacian regularization alone performed better than with energy regularization alone, especially in the case of model mismatch. Moreover, Laplacian regularization was generally less sensitive to the value of λ.
ii) RMSE was lower using joint spatial regularization than with either constraint alone. On the other hand, the CC showed only slight improvement even for the case with model mismatch. This may suggest that, at least for these relatively simple epicardial distributions, all three methods capture the basic *shape* of the epicardial potentials, but using both constraints improved amplitude recovery.
iii) The best solution found using any method and either error measure involved more regularization in the model mismatch case than in the exact model case. Moreover, in the model mismatch case the best results involved more regularization with *both* constraints and, thus, would suffer under either type of single-constraint regularization. For instance, in Table I the best result (row two, column five in the table) was only very slightly improved over using Laplacian regularization alone, and the energy regularization was quite small. On the other hand, in Table II, the best result (row seven, column six) was more significantly improved in comparison to the best result obtained using only one regularizer and the balance between the contributions of energy and Laplacian regularization was much more even.
iv) The best joint spatial solution always involved equal or smaller (usually smaller) values of the λ's than the best single-constraint solution.
v) Using RMSE as a criterion, the difference between using Laplacian regularization alone and joint spatial regularization was minimal when the Laplacian regularization parameter was large enough. However, if this parameter was even slightly smaller than "optimal," a small amount of energy regularization greatly stabilized the inverse solution. This was true with both exact and mismatched models. In the model mismatch case 1) the amount of joint energy regularization required was greater, and 2) the degree of improvement was better.

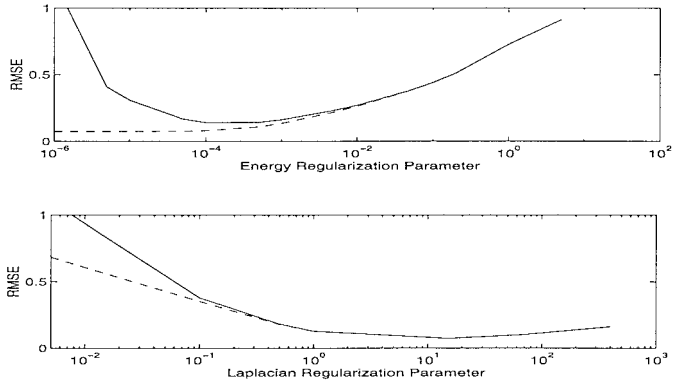

Fig. 4. RMSE as a function of the regularization parameter for the case without model mismatch. SNR = 40 dB. Top graph: Solid line for only energy regularization and dotted line for joint regularization with the Laplacian parameter fixed at the "best" value of 15. Lower graph: Solid line for Laplacian regularization only and dotted line for joint regularization with the energy regularization parameter fixed at 10^{-6}.

This last effect, i.e., the greater robustness of joint spatial regularization to under-regularizing values of either regularization parameter, is illustrated in Figs. 4 and 5. These figures show how the RMSE varies with one regularization parameter while the other is held constant. Fig. 4 is for the exact model case. In the top graph, the RMSE is plotted as a function of the energy regularization parameter when the Laplacian parameter is held constant at the optimal value, while in the bottom graph, the RMSE is shown as a function of Laplacian regularization parameter when the energy regularization parameter is held constant, again at its optimal value. Fig. 5 shows the same results for the model mismatch case. In other words, the figures

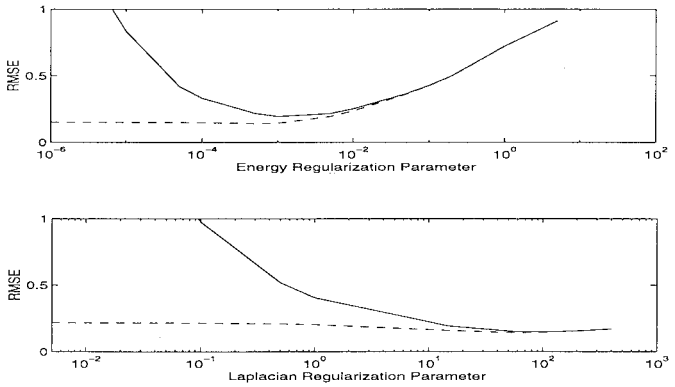

Fig. 5. Same as the previous figure for the case with model mismatch. Top part, Laplacian regularization parameter = 60. Lower part, energy regularization parameter = 10^{-4}.

show one row (top graph) and one column (bottom graph) each from Tables I and II. Clearly, the jointly regularized result was much less sensitive to under regularization, and this effect was much stronger in the model mismatch case.

b) Results using tank model: To give a visual representation of the degree and types of errors in the various reconstructions with a more realistically complex epicardial distribution, Fig. 6 shows IPM's of inverse results computed from the simulations based on the measured epicardial potentials. The results are shown for a single mid-QRS time sample from an beat initiated from a right-ventricular epicardial site, with an SNR of 30 dB. The original measured distribution is at the top of the figure. The second row shows Tikhonov zero-order reconstructions at three values of the regularization parameter, while the third row shows Tikhonov second-order reconstructions. The remaining two rows show joint spatial reconstructions using various combinations of the regularization parameter pairs. In all cases, zero-order regularization parameters are shown above and to the left of the maps and second-order parameters to the upper right. The regularization parameters were chosen to illustrate what happens with various degrees of under- or over regularization.

We will discuss these results in terms of the following five features of the original distribution specific to the distribution we selected:

i) the values and positions of maxima and minima;
ii) the accuracy of the shape of the region of negative potential around the 10–12 o'clock position (under the LAD as shown in Fig. 2);
iii) the position and density of the bundle of isocontours that mark the wavefront near the 6 o'clock position—this shows the wavefront just crossing from the right to the left ventricle as it passes under the left-anterior descending artery,
iv) the shape and density of the wavefront around 2 o'clock
v) The presence of two distinct maxima, the larger one on the anterior and the other on the posterior midline of the heart, in the broad positive region on the right side of the map.

For each item listed above we will compare the zero-order (ZO) and second-order (SO) single regularized reconstructions

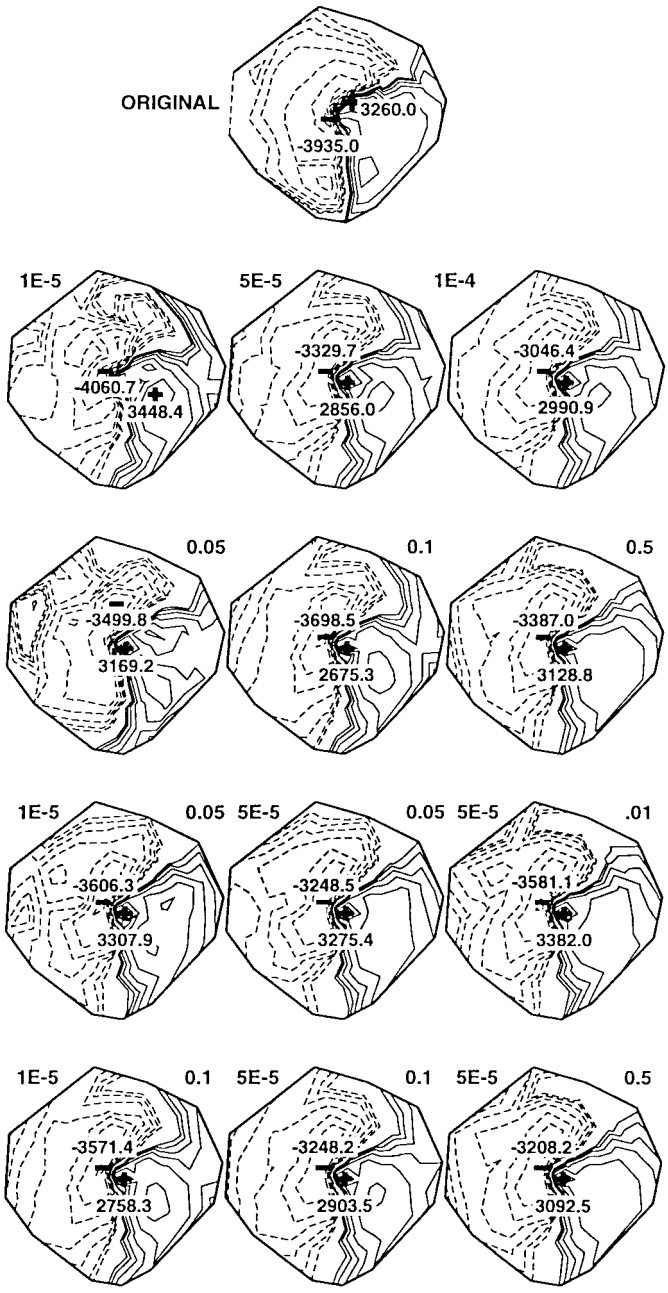

Fig. 6. IPM for one time sample of tank data at 30-dB SNR. The original distribution is on the top row. The second row shows energy regularization and the third row Laplacian regularization. The rest of the maps show joint spatial regularization. The energy regularization parameters are shown to the upper left of the maps and the Laplacian parameters to the upper right.

to the most under-regularized joint reconstruction, shown at the left of the fourth row (denoted as J1 in the sequel). (We will use λ_{ZO} and λ_{SO} to denote the ZO and SO regularization parameters respectively.) In addition we will look at the change from the lowest to middle λ_{ZO} with and without added Laplacian regularization (i.e., comparing the first and second maps of row two to those of row four). We note that many other comparisons can be made and we simply chose these to illustrate typical results and features often examined in experimental and clinical evaluation of epicardial potential maps.

i) The ZO and SO reconstructions either had difficulty locating the maximum or minimum at low values of their respective λ's or underestimated the magnitude of one or both extrema at high values of λ. The J1 reconstruction seemed to find a better compromise between amplitude and position of both maxima and minimum. Also, we note that the change in extrema amplitude with regularization parameter was smaller in the joint reconstructions than in the case of single ZO regularization.

ii) The J1 reconstruction captured the shape of the contours surrounding the negative area better than any of the single regularization reconstructions. It had more noisy spurious minima than the single regularization reconstructions with higher values of λ but less than either single regularization with its regularization parameter at the same value as in J1. Again, the reconstructions were more stable with variations in the λ_{ZO}.

iii) All of the reconstructions showed the degradation in the density of contours on the wavefront typical of regularized solutions. The SO reconstruction produced a higher density of contour lines, and was, thus, more accurate in this sense than the ZO reconstruction, but showed a marked change in shape and location, a bend to the left near the 6 o'clock position along the atrioventricular (AV) ring. The J1 reconstruction again found a compromise, more densely packed than ZO though not as densely as SO, but more accurate in position and shape than SO. The reconstructions showed only small changes with variations in λ_{ZO} in either case.

iv) The SO reconstruction of the wavefront was more accurate than ZO in both density and shape in this part of the map, and the J1 reconstruction was similar to SO. Again changes with increased λ_{ZO} were slight in both cases.

v) The J1 reconstruction found both maxima in the original map, although the locations were shifted down toward the apex and somewhat and slightly toward the left side of the heart. The SO reconstruction also found both extrema but the smaller one was more diffuse than the original, while the ZO reconstruction missed the second entirely. Increasing the ZO parameter caused even the joint reconstruction to miss the second maximum.

3) JTS Regularization: We tested the JTS method at various segments of the cardiac cycle using only the potentials from the torso tank. We used energy regularization as the spatial constraint and employed a simple high-pass filter with impulse response $\delta(n) - 0.5[\delta(n-1) + \delta(n+1)]$ (with modifications to handle edge effects). Thus, the matrix $\boldsymbol{T}$ had the form

$$\boldsymbol{T} \stackrel{\mathrm{def}}{=} \begin{bmatrix} 1 & -1 & 0 & \cdots & 0 \\ -\frac{1}{2} & 1 & -\frac{1}{2} & 0 & \cdots \\ & \ddots & \ddots & \ddots & \\ \cdots & 0 & -\frac{1}{2} & 1 & -\frac{1}{2} \\ 0 & \cdots & 0 & -1 & 1 \end{bmatrix}. \tag{20}$$

The SNR's for the tests ranged from 20 to 60 dB—results from values as low as 15 dB had an almost random appearance.

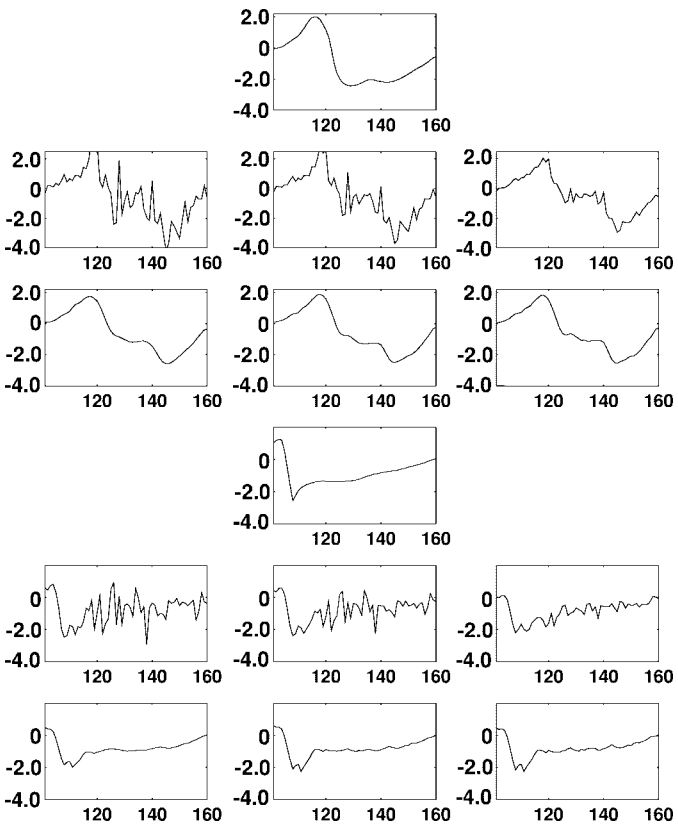

Fig. 7. JTS regularization: the effect on electrogram shape during QRS. The first and fourth rows show two selected original electrograms. The second and fifth rows show energy-only regularization and the third and sixth JTS regularization for the respective originals. For the energy regularization λ, from left to right, is 10^{-6}, 5×10^{-6}, and 10^{-5}. For the JTS regularization, the parameter pair $\underline{\boldsymbol{\lambda}}$ is (10^{-6}, 10^{-5}), (5×10^{-6}, 10^{-4}), and (10^{-5}, 5×10^{-4}).

To evaluate the effect of the number of time instants used in the augmented scheme, the intervals were varied from 5 to 60 ms, with several different SNR levels for each test. Thus, since the tank epicardial model had 64 points, the matrix size in (12) varied from 1280×1280 to 3840×3840. To calculate inverse reconstructions using 20- to 40-ms intervals we used the block Jacobi method, while for intervals longer than 40 ms we used the diagonalization method. Reconstructions using a standard block solution took several hours on a mid-level workstation when coded in MATLAB with no particular effort to optimize the code; the block Jacobi method with a 20- to 40-ms interval took several minutes, and the pre/post method only a few seconds. Single-constraint regularization on the same machine would require about 0.2–0.4 s for the same number of time samples. All results shown here are from the same epicardially paced heartbeat as the results for joint spatial regularization shown in Fig. 6.

Fig. 7 illustrates the effect on the temporal electrogram waveforms of using JTS reconstructions over temporal intervals of 60 ms during QRS at two epicardial nodes, one with a comparatively smooth time course and one with a much sharper deflection, both with an SNR of 40 dB. The 60-ms interval used in the reconstruction is shown for the first electrogram in the first row and for the electrogram with a sharper deflection in the fourth row. Rows two and three show

inverse-computed solutions for the electrogram in row one; row two contains results using only energy regularization and row three contains results with JTS regularization. The left-most plot is under-regularized, the middle plot shows L-Curve or L-Surface values, and the right plot is over-regularized. Rows five and six are the same as rows two and three but for the original electrogram in row four. In both cases, even the best regularization failed to capture all the details of the electrogram when the temporal derivative was high. But it is clear from this figure that using the JTS method we could dampen considerably the unrealistic, uncorrelated temporal behavior in the singly regularized results. In addition, the JTS results were quite insensitive to the exact choice of regularization parameter pair, in comparison to the spatially regularized solution.

To illustrate the spatial behavior of the JTS method we present IPM's for some of the JTS regularization cases described in the previous paragraph in Figs. 8 and 9. Fig. 8 focuses on two time instants during QRS (105 and 122, as illustrated by the vertical bars on the plot of the time signal at the top of the figure). The format of this figure is similar to that of Fig. 7. The original two maps are shown by themselves on the first and fourth rows, each followed by a row of three energy regularization reconstructions, and then by a row of three JTS reconstructions. The regularization parameters are also the same as in Fig. 7 and are indicated in the upper left (energy) and right (Laplacian) corner of each map. Both time instants showed considerably less variability with changing regularization parameters for JTS than purely spatial regularization. For instance, there were several spurious maxima and minima on the left ventricle (right side of the projection) at time 105 in the spatial reconstructions which were smoothed by increasing energy regularization at the cost of underestimated amplitudes. The same was true over the right ventricle in maps from time instant 112, rows five and six of Fig. 8. The JTS result was more stable across values of regularization parameters with fewer spurious local maxima and minima and less damping of the global maxima and minima. JTS regularization showed even more improvement during other segments of the cardiac cycle in which the temporal filtering of the JTS method was more helpful since the SNR was lower. Fig. 9 shows reconstructions for a sequence of the six time instants 111–116, again marked by vertical bars on the time signal plotted at the top of the figure. In this figure, the first column shows the original epicardial potentials, the second column shows inverse reconstructions using energy regularization with $\lambda = 5 \times 10^{-6}$, and the third column shows reconstructions using JTS regularization with $\underline{\lambda} = (5 \times 10^{-6}, 10^{-4})$. Although at particular time instants the energy regularization was as good as or better than the JTS regularization, there was considerable oscillatory behavior in the energy regularization that did not appear at all in the JTS results, such as the positive/negative fluctuation around the 3 o'clock position or the large jump in the global minimum at time 112 (the second row of maps). The main features of the original maps in this sequence were a) the distinct wavefront that moved slowly across the map from upper left to lower right as time progressed and separated the map into a region of positive potential on the right and bottom and one of negative potential on the upper left, and b) the pattern of one negative and two positive extrema. The JTS reconstruction provided a more accurate estimate of the location, density, and movement of the wavefront. In addition, the positive region appeared in both the original and the JTS result, in contrast to the energy regularized result.

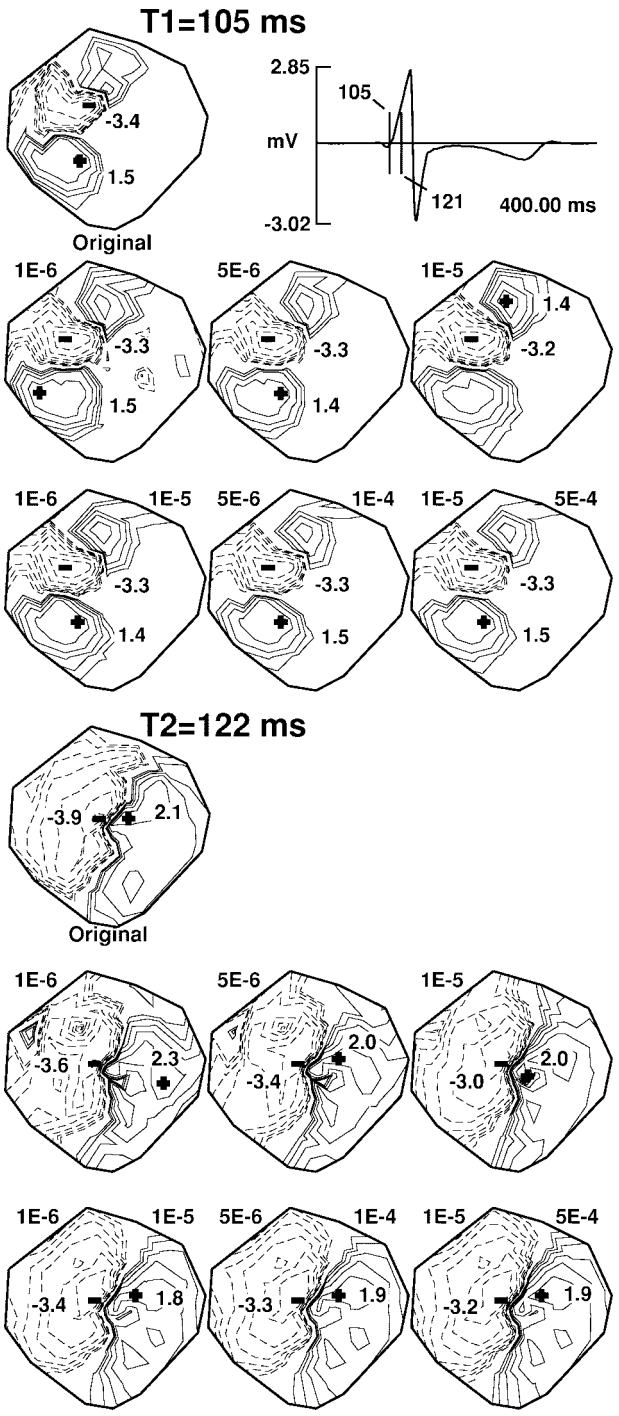

Fig. 8. IPM's for time instants 105 and 122 as show by bars in time signal plot. For format of the maps see previous figure, for layout of the figure see text. Regularization parameters match Fig. 7 and are shown to the upper left (spatial) and right (temporal) of the maps.

a) Comparison to two-step regularization: Using the block Jacobi iterative scheme to monitor the changes in

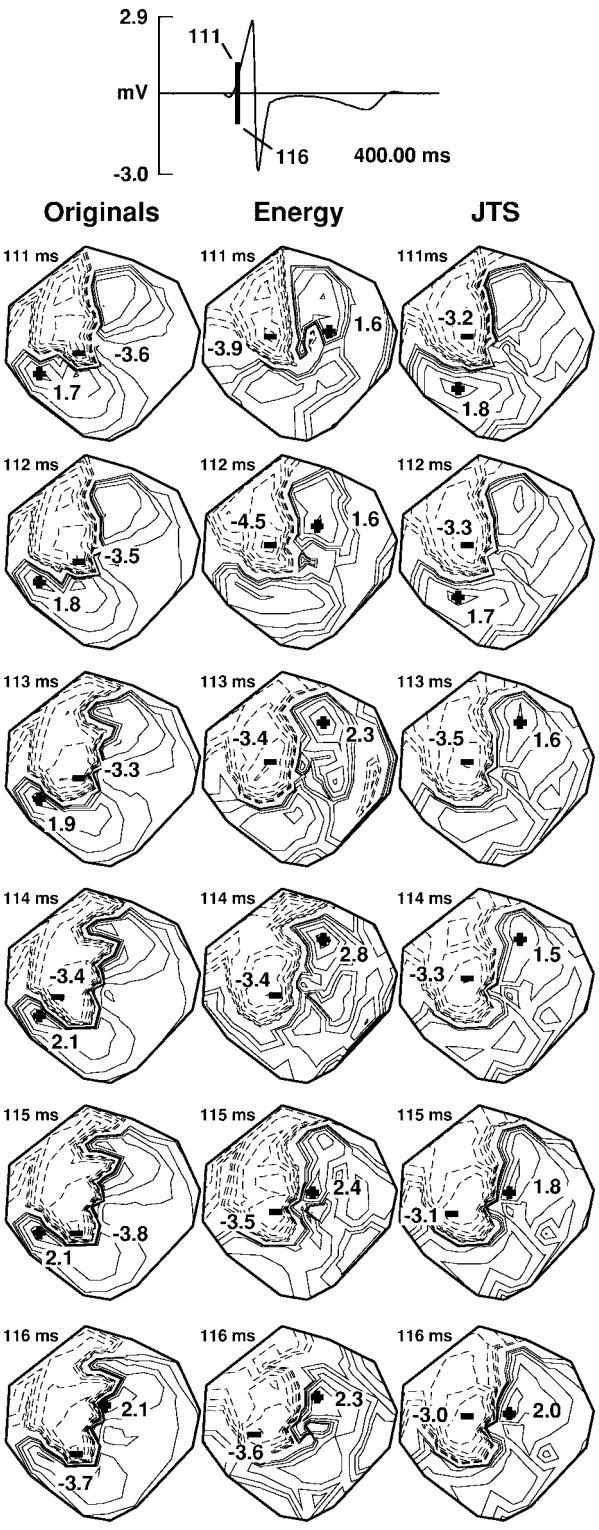

Fig. 9. IPM's for time instants 111–116 as show by bars in time signal plot. Format of the maps as in previous figures. See text for details on layout of the figure.

inverse solutions as we iteratively approached the jointly optimal solution, we observed how the results changed as the iterations proceeded. (We note again that the result after one iteration step has undergone a two-step regularization similar to that presented in [19].) Not unexpectedly given the convergence conditions in (A-1) or (A-2), we found that there was an interaction among the relative sizes of λ and η, the spatial and temporal regularization parameters, the SNR, and the rate of convergence. In general, reasonably accurate results could be achieved in several steps of the iterative algorithm when λ was close to optimal and the optimal η was small, as for instance when the interval used was entirely within the QRS complex and the SNR was, thus, comparatively high. If a smaller than optimal λ was used, even more iteration steps were required for reasonable results. When the local SNR was low (e.g., during the ST segment or at a low-amplitude epicardial node) then improvements continued until the JTS scheme had completely converged. Using global error measures, such as CC and RMSE, we rarely saw significant improvement from only one step of the algorithm. Inspection of the intermediate results, both as time signals and IPM's, revealed that generally the first few iterations were somewhat smoother in time, but at a cost in accuracy. As the algorithm iterated, temporal and spatial smoothness and accuracy were played off against each other as the optimal solution was approached.

To illustrate these results, in Fig. 10 both temporal plots of three leads and IPM's at two time instants are shown. The parameters of the simulation were the same as for the previous two figures, except that only 20 time instants, rather than 60, were included in the optimization, so that the final result did not correspond exactly to that in the previous figures. Convergence was reached after 274 iterations. In the top half of the figure, the upper left-hand panel contains the original signal at node 47, with vertical bars marking the interval shown in the other panels. Each of the other three panels shows four inverse calculated waveforms for each of three nodes; one obtained with only spatial (energy) regularization, one each after one and four iterations of the block Jacobi algorithm, and the fourth after convergence. In each panel, the smooth solid line is the original epicardial signal and the jagged solid line the spatially regularized reconstruction. The dotted line is the reconstruction after one iteration, the dashed line is after four iterations, and the dot-dashed line is the reconstruction after convergence. We note that the solution after the first iteration was quite smooth in time, but was also less able to follow more rapid variations in the temporal waveform than the converged solution.

In the bottom half of this figure, we show IPM's for two time instants within the interval shown in the top half, denoted as 112 and 113 ms and corresponding to two of the time samples shown in Fig. 9. The correct solution and the solution found with only spatial regularization can be seen in this latter figure: in Fig. 10 we show results after one, four, and 50 iterations and at convergence. As the algorithms iterated we saw minor but significant improvements in accuracy, both in terms of amplitudes and in terms of the details of the distribution, especially the shape and density of the bundles of isocontours that mark the location of the activation wavefront (see, for instance, the region near the 8 o'clock position) and the locations of maxima and minima (for example, the leftward shift of the local maxima near the 6 o'clock position).

b) Effect of the interval length L: We tested the effect of varying interval lengths in the JTS scheme by holding the filter

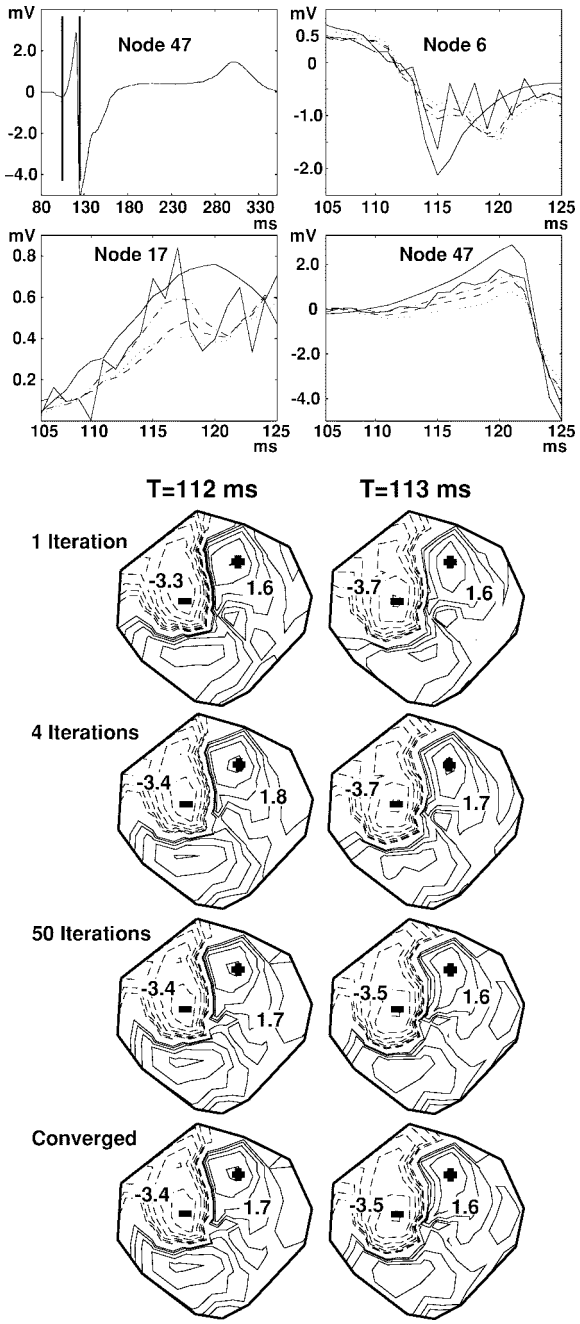

Fig. 10. Electrograms and IPM's at various iterations of the block Jacobi solver. The top four panels show reconstructions at three nodes for 20 ms (time instants 105–124 as shown by the bars on the top left graph). The curves are identified in the text. The bottom eight panels show IPM's for time instants 112 and 113. Format as in previous figure. See text for details.

length constant and letting L range from 5 to 60 ms; a larger L meant a longer interval over which the weighted sum of the three norms was minimized. We generally saw improvement over single time instant regularization for intervals in the range of 10–60 ms, with no clear "best" length. An example comparison can be made by contrasting the results in Fig. 9 for time instants 112 and 113 with the corresponding fully converged results in Fig. 10. For instance, at time 112 the amplitudes of the two local maxima were more accurately reproduced in the former figure (with $L = 60$) than in the latter (with $L = 20$). In particular, with the smaller value of L the maximum near the 8 o'clock position was underestimated, an example of a more general tendency noted below.

It was difficult to draw definitive conclusions from these tests and we consider future development of a method to determine a good interval length to be a priority. Results were generally better with longer segments during low SNR parts of the cycle such as the ST segment, but better with shorter segments when the interval included parts of the cycle with distinct temporal characteristics (such as the QRS complex and the ST region), suggesting that there may be an interaction between the interval length used and the type of filter employed, another topic of future research. We also observed that JTS regularization over longer intervals seemed to be able to reconstruct both maximum and minimum amplitudes more accurately across a wavefront without the instability and temporal oscillation present with spatial regularization alone. Shorter intervals seemed to often capture one extremum while smoothing the other. We speculate this may happen because we are minimizing two-norms and the longer temporal interval may allow a greater local excursion of the spatial amplitudes without affecting the overall combined norm as much.

V. Conclusions and Future Work

In Section I, we listed three motivations for exploring the use of more than one simultaneous regularizing constraint. In evaluating the results of our tests we found the following.

1) Our conjecture that we might be able to take advantage of the "reasonableness" of both constraints when two constraints were imposed jointly was upheld, in particular by the results of the experiments using JTS regularization with the tank data. We were able to successfully dampen unrealistic noise in inverse solutions while simultaneously regularizing against spatial sensitivity to noise.
2) Our conjecture that using two regularization constraints jointly would decrease dependence on a particular constraint and generally require smaller values of the corresponding regularization parameters was also upheld. The optimal regularization values as determined using our extended L-Surface approach when applied to both dipole simulation data and measured potentials supported this hypothesis.
3) Furthermore, the conjecture that using two constraints would increase robustness to error in the value of regularization parameters was also upheld. This was evident in the behavior of the L-Surface near its corner in comparison to the corner of the L-Curve and in the results of the dipole and tank model experiments.
4) Temporal behavior of the electrograms was generally much more realistic using the JTS method than with spatial regularization alone, and more accurate than simply post-filtering spatially regularized estimates. If temporal characteristics of the resulting estimates are important, for instance to estimate activation or recovery times, then use of temporal constraints could be very useful.

In the process of developing and testing these methods we performed the following:

1) introduced the L-Surface as an extension to the L-Curve for the purpose of evaluating candidate regularization parameter pairs for two constraints;
2) found that joint spatial regularization with Laplacian and energy constraints showed some improvement in the inverse solution over single-parameter regularization, but that the most significant contribution was increased robustness to the exact choice of regularization parameters, especially for under-regularized solutions;
3) found that JTS regularization significantly improved the accuracy of the temporal behavior of the inverse solution as compared to spatial regularization only:
4) developed efficient schemes to solve the JTS equation under certain mild conditions;
5) compared results from the dipole simulations between i) inverse solutions computed when the same model is used to generate the data via a forward solution as is used in the inverse solution, and ii) inverse solutions computed when there is a mismatch between the model used to generate the forward data and that used in the inverse solutions. We found the expected result that in the case of mismatch between forward and inverse models, at least for dipole simulations, more regularization was required than when the correct forward model was used in the inverse solution. We also found the unanticipated result that in the model mismatch case joint spatial regularization provided considerably more improvement over either regularization alone than it did in the exact model case;
6) found that a significant percentage of the improvement over spatial regularization achieved by the JTS scheme, when implemented in an iterative fashion, came after the first iteration, indicating that spatial regularization followed by simple post-filtering temporal regularization is often not close to the optimal JTS regularization;
7) found that for some regularization parameters there is significant degradation compared to intermediate iterates if the block Jacobi algorithm is allowed to iterate to full convergence, even though the result at convergence is better than with no temporal regularization or with only one iteration of temporal filtering. This is due to residual illconditioning of the block matrix used in the iteration and suggests the possibility of additional regularization via truncation of the iterations, as in [8] and [15].

Current work is proceeding in the following areas:

1) acquiring tank data with measured epicardial and body surface potentials and geometry to enable testing of the effects of model mismatch in a more realistic scenario;
2) further analysis of joint spatial and JTS regularization via modified simultaneous diagonalization techniques;
3) further study of more detailed questions regarding the application of the JTS method. For instance, we are studying ways to find an optimal interval length for the JTS method, looking at the effect of using different filters in the JTS matrix $\boldsymbol{T}$, and exploring the effects of space-varying and time-varying JTS schemes.

APPENDIX
CONVERGENCE ANALYSIS OF BLOCK JACOBI METHOD

As stated in Section III-C.1, the iterative scheme described is a block Jacobi method [32], and, in analogy to "scalar" Jacobi iterative methods, which require diagonal dominance of the system matrix for convergence, here the matrix $\overline{\boldsymbol{B}}$ has to have *block* diagonal dominance. This is guaranteed if the maximum over all i for any induced matrix norm $\|\cdot\|$ satisfies the condition

$$\|\boldsymbol{B}_{ii}^{-1}\| \sum_{j\neq i} \|\boldsymbol{B}_{ij}\| \leq 1. \tag{A-1}$$

If the spatial regularization is Tikhonov zero order, and we take $\|\cdot\|$ as the induced two-norm, this condition reduces to

$$\frac{\eta^2}{\sigma_N^2+\lambda^2+\eta^2 r_{h_0}} \sum_{j\neq i} |r_{h_{i-j}}| \leq 1, \qquad \forall i \tag{A-2}$$

where $r_{h_{i-j}}$ are the $\{i,j\}$ elements of the Toeplitz $L\times L$ correlation matrix $\boldsymbol{T}^T\boldsymbol{T}$ and σ_N is the smallest nonzero singular value of the matrix $\boldsymbol{A}$. If we let $\gamma=\eta/\lambda$ and assume that σ_N is small, relative to the spatial regularization parameter λ and, thus, $(\sigma_N^2/\lambda^2)\ll 1$, we can approximate the condition by the simple expression

$$\frac{\gamma^2}{1+\gamma^2 r_{h_0}} \sum_{j=0, j\neq i}^{L-1} |r_{h_{i-j}}| \leq 1. \tag{A-3}$$

A. Details of Pre/Post Diagonalization Method

Proceeding from (19), if $\boldsymbol{R}=\boldsymbol{I}$, $\boldsymbol{P}$ and $\boldsymbol{S}$ can be decomposed using the SVD as

$$\boldsymbol{P}=\boldsymbol{V}_A\,(\Sigma_A^2+\lambda^2\boldsymbol{I})\boldsymbol{V}_A^T \tag{A-4}$$

and

$$\boldsymbol{S}=\boldsymbol{V}_T\Sigma_T^2\boldsymbol{V}_T^T \tag{A-5}$$

where $\boldsymbol{V}_A$ and $\boldsymbol{V}_T$ are the right singular matrices of $\boldsymbol{A}$ and $\boldsymbol{T}$ respectively. The singular values of $\boldsymbol{P}$ are $(\sigma_1^2+\lambda^2,\sigma_2^2+\lambda^2,\cdots,\sigma_N^2+\lambda^2)$, where the σ_i are the singular values of $\boldsymbol{A}$, and Σ_T^2, the singular value matrix of $\boldsymbol{S}$, is $(\mathrm{diag}(\eta^2\sigma_{T_1}^2,\eta^2\sigma_{T_2}^2,\cdots,\eta^2\sigma_{T_L}^2))$, with σ_{T_i} the singular values of $\boldsymbol{T}$. Let

$$\boldsymbol{Q}=\boldsymbol{V}_A^T\boldsymbol{Z}\boldsymbol{V}_T \tag{A-6}$$

and

$$w_{ij}=\frac{q_{ij}}{\sigma_i^2+\lambda^2+\eta^2\sigma_{T_j}^2} \tag{A-7}$$

for $i=1,2,\cdots,N$ and $j=1,2,\cdots,L$, where u_{ij} denotes the $\{i,j\}$ element of a matrix $\boldsymbol{U}$. Then the solution to the joint regularization equation is

$$\boldsymbol{H}=\boldsymbol{V}_A\boldsymbol{W}\boldsymbol{V}_T^T. \tag{A-8}$$

As noted in the text, if $\boldsymbol{R}\neq\boldsymbol{I}$ we would need to decompose the matrix $\boldsymbol{P}$ separately for each value of λ.

ACKNOWLEDGMENT

The authors would like to thank B. Shafai and D. Burgess for bringing [32] and [33], respectively, to their attention.

REFERENCES

[1] B. Taccardi, "Distribution of heart potentials on the thoracic surface of normal human subjects," *Circ. Res.*, vol. 12, pp. 341–352, 1963.
[2] D. M. Mirvis, "Methods for body surface electrocardiographic mapping," *Body Surface Electrocardiographic Mapping*, in D. M. Mirvis, Ed. Boston, MA: Kluwer, 1988, pp. 43–62.
[3] D. B. Geselowitz, "On the theory of the electrocardiogram," *Proc. IEEE*, vol. 77, June 1989.
[4] Y. Rudy and B. J Messinger-Rapport, "The inverse problem in electrocardiography: Solutions in terms of epicardial potentials," *CRC Crit. Rev. in Biomed. Eng.*, vol. 16, pp. 215–268, 1988.
[5] R. M. Gulrajani, F. A. Roberge, and P. Savard, "The inverse problem of electrocardiography," *Comprehensive Electrocardiology*, in P. W. Macfarlane and T. D. Veitch Lawrie, Eds. Oxford, U.K.: Pergamon, vol. pp. 237–288, 1989.
[6] C. W. Groetsch, *The Theory of Tikhonov Regularization for Fredholm Equations of the First Kind*. Boston, MA: Pitman, 1984.
[7] A. Tikhonov and V. Arsenin, *Solution of Ill-Posed Problems*. Washington, DC: Winston, 1977.
[8] P. C. Hansen, "Regularization, GSVD and truncated GSVD," *BIT*, vol. 29, pp. 491–504, 1989.
[9] B. J. Messinger-Rapport and Y. Rudy, "Regularization of the inverse problem in electrocardiography: A model study," *IEEE Trans Biomed Eng*, vol. 35, p. 89, 1988.
[10] ———, "Computational issues of importance to the inverse recovery of epicardial potentials in a realistic heart-torso geometry," *Math. Biosci.*, vol. 97, pp. 85–120, 1989.
[11] P. Colli-Franzone, L. Guerri, S. Tentonia, C. Viganotti, S. Spaggiari, and B. Taccardi, "A numerical procedure for solving the inverse problem of electrocardiography. Analysis of the time-space accuracy from *in vitro* experimental data," *Math Biosci*, vol. 77, p. 353, 1985.
[12] P. C. Hansen, "Analysis of discrete ill-posed problems by means of the L-curve," *SIAM Rev.*, vol. 34, no. 4, pp. 561–580, 1992.
[13] D. H. Brooks, G. M. Maratos, G. Ahmad, and R. S. MacLeod, "The augmented inverse problem of electrocardiography: Combined time and space regularization," in *Proc. IEEE Engineering in Medicine and Biology Society 15th Annu. Int. Conf.*, 1993, pp. 773–774.
[14] V. Shahidi, P. Savard, and R. Nadeau, "Forward and inverse problem of electrocardiogography: Modeling and recovery of epicardial potentials in humans," *IEEE Trans. Biomed. Eng.*, vol. 41, pp. 249–256, Mar. 1994.
[15] D. H. Brooks, G. Ahmad, and R. S. MacLeod, "Multiply constrained inverse electrocardiography: Combining temporal, multiple spatial, and iterative regularization," in *Proc. 16th Ann. Int. Conf. IEEE EMBS*, 1994.
[16] R. S. MacLeod, *Percutaneous Tranluminal Coronary Angioplasty as a Model of Cardiac Ischemia: Clinical and Modeling Studies*, Ph.D. dissertation. Halifax, N.S., Canada: Dalhousie Univ., 1990.
[17] C. R. Johnson and R. S. MacLeod, "Inverse solutions for electric and potential field imaging," in *Physiological Imaging, Spectroscopy, and Early Diagnostic Methods*, R. L. Barbour and M. J. Carvlin, Eds. Philadelphia, PA: SPIE, 1993.
[18] R. D. Throne and L. G. Olson, "A truncated eigenvector solution to the inverse problem of electrocardiography," in *Proc. IEEE Engineering in Medicine and Biology Society 15th Annu. Int. Conf.*, IEEE Press, 1993, pp. 771–772.
[19] H. S. Oster and Y. Rudy, "The use of temporal information in the regularization of the inverse problem in electrocardiography," *IEEE Trans. Biomed. Eng.*, vol. 39, pp. 65–75, Jan. 1992.
[20] J. J. M. Cuppen and A. van Oosterom, "Model studies with the inversely calculated isochrones of ventricular depolarization," *IEEE Trans.Biomed. Eng.*, vol. BME-31, pp. 652–659, 1984.
[21] F. Greensite, "Well-posed formulation of the inverse problem of electrocardiography," *Ann. Biomed. Eng.*, vol. 22, pp. 172–183, 1994.
[22] D. H. Brooks, C. L Nikias, and J. H. Siegel, "An inverse solution in electrocardiography in the frequency domain," in *Proc. IEEE EMBS 15th Annu. Int. Conf.*, 1988, pp. 970–971.
[23] R. C. Barr, T. C. Pilkington, J. P. Boineau, and C. L. Rogers, "An inverse electrocardiographic solution with an on-off model," *IEEE Trans. Biomed. Eng.*, vol. BME-17, pp. 49–56, 1970.
[24] D. Joly, Y. Goussard, and P. Savard, "Time-recursive solution to the inverse problem of electrocardiography: A model-based approach," in *IEEE EMBS 15th Annu. Int. Conf.*, 1993, pp. 767–768.
[25] J. El-Jakl, F. Champagnat, and Y. Goussard, "Time-space regularization of the inverse problem of electrocardiography," in *Proc. 17th Annu. Int. Conf. IEEE EMBS*, 1995.
[26] G. Ahmad, D. H. Brooks, G. Maratos, and R. S. MacLeod, "Joint energy and Laplacian regularization in inverse electrocardiography," in *Proc. 20th N.E. Bioeng. Conf.* Springfield, MA, 1994, pp. 59–61.
[27] Y. Yamashita, "Theoretical studies on the inverse problem in electrocardiography and the uniqueness of the solution," *IEEE Trans Biomed Eng*, vol. BME-29, pp. 719–725, 1982.
[28] R. M. Gulrajani, P. Savard, and F. A. Roberge, "The inverse problem in electrocardiography: Solutions in terms of equivalent sources," *CRC Crit. Rev. Biomed. Eng.*, vol. 16, pp. 171–214, 1988.
[29] R. Plonsey, "Laws governing current flow in the volume conductor," in *The Theoretical Basis of Electrocardiology*, C. V. Nelson and D. B. Geselowitz, Eds. Oxford, U.K.: Clarendon, 1976, pp. 165–174.
[30] R. C. Barr, M. Ramsey, and M. S. Spach, "Relating epicardial to body surface potential distributions by means of transfer coefficients based on geometry measurements," *IEEE Trans. Biomed. Eng.*, vol. BME-24, pp. 1–11, 1977.
[31] P. C. Hansen, "Regularization tools, a matlab package for analysis and solution of discrete ill-posed problems," Tech. rep., UNI.C, DK-2800 Lyngby, Denmark, June 1992.
[32] I. K. Argyros and F. Szidarovszky, *The Theory and Applications of Iteration Methods*. Ann Arbor, MI: CRC, 1993.
[33] A. Jameson, "Solution of the equation $AX + XA = C$ by inversion of an $M \times M$ or $N \times N$ matrix," *SIAM J. Appl. Math.*, vol. 16, pp. 1020–1023, 1968.
[34] R. S. MacLeod, B. Taccardi, and R. L. Lux, "Mapping of cardiac ischemia in a realistic torso tank preparation," in *Proc. XXIInd Annu. Meeting Int. Congress on Electrocardiography* , May 1995.
[35] M. S. Spach and C. R. Barr, "The use of isopotential surface maps in understanding clinical ECG's," *Amer. J. Dis. Child*, vol. 124, pp. 359–363, 1972.
[36] G. F. Ahmad, "Inverse electrocardiography by simultaneous and iterative imposition of multiple constraints," Ph.D. dissertation, Northeastern Univ., Boston, MA, 1995.
[37] T. F. Oostendorp, A. van Oosterom, and G. Huiskamp, "Interpolation on a triangulated 3d surface," *J. Computational Phys.*, vol. 80, pp. 331–343, 1989.

Dana H. Brooks (S'86–M'91) received the B.A. degree in english in 1972 from Temple University, Philadelphia, PA, and the B.S.E.E (1986), M.S.E.E (1988), and Ph.D. (1991) degrees in electrical engineering from Northeastern University, Boston, MA.

He is currently an Associate Professor of Electrical and Computer Engineering, Associate Director of the Center for Communications and Digital Signal Processing, and PI of the Biomedical Signal Processing Laboratory, at Northeastern University. His research interests are in statistical and digital signal processing, with particular application to biomedical problems. Specific current interests include inverse problems in electrocardiography, multiresolution analysis and segmentation of cardiac electrical maps, adaptive dynamic MRI, and acousto-photonic imaging.

Ghandi F. Ahmad received the B.Sc. degree in 1984 in electrical engineering with High Honors from the University of Illinois at Chicago and the M.S.E.E. (1986) and Ph.D. (1995) degrees in electrical engineering from Northeastern University, Boston, MA.

Since 1995 he has been teaching in the Electronics Engineering Department at Al-Quds University in Jerusalm, Israel. He is currently Chairman of the Electronics Engineering Department at Al-Quds University. His research interests include digital signal processing and detection and estimation with applications to inverse problems, and biomedical signal processing.

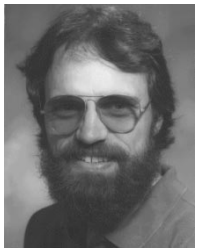

Robert S. MacLeod (S'87–M'87) received both the B.Sc. (1979) degree in engineering physics and the Ph.D. (1990) degree in physiology and biophysics from Dalhousie University, Halifax, N.S. Canada. He received the M.Sc. degree in electrical engineering came from the Technische Universität, Graz, Austria, in 1985.

He is an Assistant Professor in the Department of Internal Medicine (Division of Cardiology) and Department of Bioengineering at the University of Utah, Salt Lake City, and a member of the Nora Eccles Harrison Cardiovascular Research and Training Institute. His research interests include computational electrocardiography (forward and inverse problems), experimental investigation and clinical detection of cardiac ischemia and repolarization abnormalities, and scientific computing and visualization.

George M. Maratos received the M.S.E.E. degree from Northeastern University, Boston, MA, in 1992.